



# Octahedral Co<sub>3</sub>O<sub>4</sub>/carbon nanofiber composite-supported Pt catalysts for improved methanol electrooxidation



HyeLan An, Geon-Hyoung An, Hyo-Jin Ahn \*

Department of Materials Science and Engineering, Seoul National University of Science and Technology, Seoul 139-743, Republic of Korea

## ARTICLE INFO

### Article history:

Received 16 April 2015

Received in revised form 11 May 2015

Accepted 12 May 2015

Available online 19 May 2015

### Keywords:

Octahedral Co<sub>3</sub>O<sub>4</sub>/CNF composites

Pt catalysts

Electrospinning

A hydrothermal method

Methanol electrooxidation

Electrocatalytic stability

## ABSTRACT

Octahedral Co<sub>3</sub>O<sub>4</sub>/carbon nanofibers (CNFs) composite-supported Pt catalysts are synthesized using electrospinning, hydrothermal, and reduction methods in sequence, and their structure, chemical bonding states, and electrochemical properties are investigated. To obtain the optimal support, the relative molar ratio of the Co precursor to the solution was adjusted to three different levels: 0.05 M (sample A), 0.1 M (sample B), and 0.2 M Co precursor (sample C). Sample B exhibited the highest electrocatalytic activity of ~415.6 mA mg<sub>Pt</sub><sup>-1</sup> and superb electrocatalytic stability compared to commercial Pt/C, Pt/conventional CNFs, sample A, and sample C. This performance improvement can be explained by the combined effects of optimally sized octahedral Co<sub>3</sub>O<sub>4</sub> on the CNF matrix, resulting in the maximum dispersion of Pt catalysts, and the formation of Co(OH)<sub>2</sub> phases, which hinder CO poisoning.

© 2015 Elsevier B.V. All rights reserved.

## 1. Introduction

Direct methanol fuel cells (DMFCs) consist of four main components: an anode, a cathode, an electrolyte, and a separating membrane. They are of considerable interest as power sources in portable electronic devices (i.e., mobile homes, boats, cabins, and laptops) because of advantages such as high energy density, high methanol conversion efficiency, ease of storage, low operation temperature, rapid start-up, and low environmental toxicity [1,2]. Despite these advantages, DMFCs have major disadvantages such as the high cost of Pt catalysts, poor durability caused by CO poisoning, and methanol crossover. Among them, the use of expensive Pt catalysts is the most important obstacle for the industrialization of DMFCs. To overcome this problem, one strategy is to introduce supporting materials that hinder CO poisoning and lower the amount of Pt loading needed. In general, supported Pt catalysts demonstrate improved electrocatalytic activity and high electrocatalytic stability compared to unsupported Pt catalysts [3].

Until now, supporting materials such as carbon-based systems (graphene, carbon nanotubes (CNTs), carbon nanofibers (CNFs)), non carbon-based systems (TiO<sub>2</sub>, TiN, SnO<sub>2</sub>, SiO<sub>2</sub>, ITO, WO), and hybrid-based systems consisting of carbon and non-carbon (graphene-ITO, graphene-CeO<sub>2</sub>, CNT-CeO<sub>2</sub>, carbon-WO<sub>3</sub>) have been reported [3–5]. In particular, hybrid supports to improve the

electrocatalytic activity in DMFCs has attracted considerable attention because of the excellent electrical conductivity of carbon as well as the superior electrocatalytic stability of non-carbon. For example, Zeng et al. synthesized the ordered mesoporous carbon (OMCs)-WO<sub>3</sub> composite-supported Pt catalysts by carbonization and thermal decomposition methods, which showed excellent catalytic activity (410 mA mg<sup>-1</sup>) [4]. Wang et al. reported on the graphene-CeO<sub>2</sub> hybrid composite-supported Pt catalysts, which exhibited a superb catalytic activity (366 mA mg<sub>Pt</sub><sup>-1</sup>) with good electrocatalytic stability [5]. However, hybrid supports on octahedral Co<sub>3</sub>O<sub>4</sub>/CNF composites have not been reported hitherto for enhanced methanol electrooxidation in DMFCs.

In this study, we successfully synthesized octahedral Co<sub>3</sub>O<sub>4</sub>/CNF composite-supported Pt catalysts for use as anodes in DMFCs. To obtain the best performance, we varied the sizes of octahedral Co<sub>3</sub>O<sub>4</sub> on the CNF matrix using three different experimental conditions. Co<sub>3</sub>O<sub>4</sub> as a part of the hybrid composite supports for Pt catalysts are chosen because of advantages such as high catalytic activity in DMFCs, inhibition of CO poisoning, low cost, and good corrosion stability as well as the use for electrochemical fields including fuel cells, photo-catalysts, and water oxidation catalysts [6–8].

## 2. Experiments

### 2.1. Synthesis of octahedral Co<sub>3</sub>O<sub>4</sub>/CNF composite-supported Pt catalysts

Three types of octahedral Co<sub>3</sub>O<sub>4</sub>/CNF composite-supported Pt catalysts were synthesized by sequentially using electrospinning, hydrothermal, and reduction methods. For all the samples, Co-seed-embedded CNFs were prepared using

\* Corresponding author. Tel.: +82 029706622; fax: +82 029736657.

E-mail address: [hjahn@seoultech.ac.kr](mailto:hjahn@seoultech.ac.kr) (H.-J. Ahn).

one-pot electrospinning for uniform growth of octahedral  $\text{Co}_3\text{O}_4$  on the CNFs. Briefly, cobalt nitrate ( $\text{Co}(\text{NO}_3)_2 \cdot 6\text{H}_2\text{O}$ ) was added to a solution consisting of polyacrylonitrile (PAN,  $M_w = 150,000 \text{ g mol}^{-1}$ ), poly(vinylpyrrolidone) (PVP,  $M_w = 1,300,000 \text{ g mol}^{-1}$ ), and N,N-Dimethylformamide (DMF). The solution was loaded into a plastic syringe equipped with a 23-gauge needle. For the electrospinning process, the feeding rate and high voltage were fixed at  $0.03 \text{ mL h}^{-1}$  and 16 kV, respectively, with a syringe needle-to-collector distance of 15 cm. Afterwards, the as-spun nanofibers were stabilized at  $280^\circ\text{C}$  for 2 h in air and subsequently carbonized at  $800^\circ\text{C}$  for 2 h in a  $\text{N}_2$  atmosphere.

To obtain three different sizes of octahedral  $\text{Co}_3\text{O}_4$  by using a hydrothermal method, the relative molar ratio of the Co precursor to the solution was controlled to be 0.05, 0.1, and 0.2 M, respectively. Co-seed-embedded CNFs, prepared as described above using cobalt nitrate as a precursor, and cetyltrimethylammonium bromide (CTAB) as a surfactant were dissolved in methanol/deionized (DI) water (5:1 v/v). After stirring for 2 h, the above-mentioned solution was put into a Teflon lined stainless steel autoclave, and then maintained at  $180^\circ\text{C}$  for 24 h. The resultant samples were washed several times with DI water and then dried at  $80^\circ\text{C}$ . Finally, the three different types of supports were dispersed in a  $0.56 \text{ mM H}_2\text{PtCl}_6 \cdot x\text{H}_2\text{O}$  solution and reduced by  $\text{NaBH}_4$  to load 20 wt% Pt catalysts. All the samples were washed using DI water and then freeze-dried at  $-50^\circ\text{C}$  to synthesize metallic Pt catalysts. We successfully synthesized three different types of octahedral  $\text{Co}_3\text{O}_4/\text{CNF}$  composite-supported Pt catalysts. For comparison, conventional CNF-supported Pt catalysts without cobalt nitrate precursor and commercial Pt/C (20 wt% Pt on Vulcan XC-72R) were prepared. Thus, 20 wt% Pt catalysts supported on conventional CNFs and on three different levels of supports (0.05, 0.1, and 0.2 M Co precursor) are herein referred to as Pt/conventional CNFs, sample A, sample B, and sample C, respectively.

## 2.2. Characterization

The morphological and structural properties of the samples were examined by field emission-scanning electron microscopy (FE-SEM; Hitachi S-4800) and transmission electron microscopy (TEM; FEI Tecnai  $\text{C}^2$ , KBI Gwangju Center). To identify the composition of constituent elements, TEM-EDS mapping (Phillips CM20T/STEM) with an energy-dispersive X-ray spectrometer was performed. The crystallinities and chemical bonding states of the samples were determined by X-ray diffraction (XRD; Rigaku D/Max-2500 with  $\text{Cu K}\alpha$  radiation in the range of  $10\text{--}90^\circ$ ) and X-ray photoelectron spectroscopy (XPS; Thermo Electron ESCALAB250 with  $\text{Al K}\alpha$  X-ray source). The electrochemical properties were investigated using a potentiostat/galvanostat (Ecochemie Autolab PGST302N, Netherlands) in a conventional three-electrode system including a working electrode (glassy carbon electrode, area =  $0.07 \text{ cm}^2$ ), a counter electrode (Pt gauze), and a reference electrode ( $\text{Ag}/\text{AgCl}$ , sat. KCl). The electrolyte was prepared by mixing  $0.5 \text{ M H}_2\text{SO}_4$  and  $2 \text{ M CH}_3\text{OH}$  under purging Ar gas. The cyclic voltammograms were obtained at a scan rate of  $50 \text{ mV s}^{-1}$  in the range  $-0.2$  to  $1.0 \text{ V}$  to measure electrocatalytic activity during methanol electrooxidation. Chronoamperometry measurements were performed at a constant potential of  $0.5 \text{ V}$  for 1500 s to investigate the stability of the catalysts.

## 3. Results and discussion

Fig. 1a–e shows FESEM images obtained from conventional CNFs, Pt/conventional CNFs, sample A, sample B, and sample C, respectively. The average diameters of the CNFs are  $\sim 257$  to  $\sim 308 \text{ nm}$  for conventional CNFs,  $\sim 264$  to  $\sim 308 \text{ nm}$  for Pt/conventional CNFs,  $\sim 295$  to  $316 \text{ nm}$  for sample A,  $\sim 281$  to  $\sim 342 \text{ nm}$  for sample B, and  $\sim 285$  to  $\sim 358 \text{ nm}$  for sample C. The diameters of samples A–C are larger than that of the Pt/conventional CNFs due to the existence of Co seeds within the CNF matrix. In addition, conventional CNFs (Fig. 1a) exhibit a smooth NF surface. However, for Pt/conventional CNFs, agglomerated Pt blobs are observed as shown in Fig. 1b. Furthermore, samples A–C exhibit octahedral  $\text{Co}_3\text{O}_4$  architectures grown on the CNFs. To achieve the optimum size of octahedral  $\text{Co}_3\text{O}_4$ , we tested three molar ratios of the Co precursor to the solution (0.05 M, 0.1 M, and 0.2 M). As shown in Fig. 1c–e, the lower the molar concentration of the Co precursor, the smaller the size of octahedral  $\text{Co}_3\text{O}_4$ . In particular, sample B (Fig. 1d) demonstrated uniformly grown optimally sized octahedral  $\text{Co}_3\text{O}_4$  ( $288\text{--}469 \text{ nm}$  in size) on the CNF matrix, which could result in improved methanol electrooxidation in DMFCs.

Fig. 2 shows TEM images (a–e) and enlarged TEM images (Fig. 2f–j) of Pt/conventional CNFs, sample A, sample B, and sample

C. As shown in Fig. 2a, the Pt/conventional CNFs display a uniform bright-gray contrast, attributed to the CNF matrix, and sparsely distributed small dark spots, corresponding to the Pt nanoparticles. Fig. 2b shows Co-seed-embedded CNFs fabricated by one-pot electrospinning, which consist of dark spots corresponding to Co nanoparticles and a bright-gray contrast related to the CNF matrix. Samples A–C (Fig. 2c–e) exhibit three different types of octahedral  $\text{Co}_3\text{O}_4$  architectures grown on the Co-seed-embedded CNFs using a hydrothermal method. They are composed of small-sized Pt nanoparticles ( $3\text{--}5 \text{ nm}$  in size) supported on octahedral  $\text{Co}_3\text{O}_4/\text{CNF}$  composites. In particular, samples A–C exhibit excellent dispersion of Pt nanoparticles on the supports compared to the Pt/conventional CNFs, as shown in Fig. 2h–j. Furthermore, sample B exhibits optimally sized octahedral  $\text{Co}_3\text{O}_4$  grown on the CNF matrix, which results in the maximum dispersion of Pt catalysts, among all the supports. Fig. 2k shows the TEM-EDS mapping data for octahedral  $\text{Co}_3\text{O}_4/\text{CNF}$  composite-supported Pt catalysts to examine the dispersion of Pt atoms on the supports. The EDS results indicate that Pt atoms on the supports are uniformly distributed on the octahedral  $\text{Co}_3\text{O}_4$  architectures as well as on the CNF matrix.

Fig. 3a shows the XRD plots obtained for all the samples. The reference lines shown below are the standard data for a pure Pt (JCPDS card No. 04–0802), a pure Co (JCPDS card No. 15–0806), and a pure  $\text{Co}_3\text{O}_4$  (JCPDS card No. 78–1970). The Pt/conventional CNFs and Co-seed-embedded CNFs exhibit broad diffraction peaks at  $2\theta = \sim 25^\circ$ , indicating the presence of graphite with (002) layer. For Co-seed-embedded CNFs, the (111) and (200) planes can be attributed to the peaks at  $2\theta = 44.2^\circ$  and  $51.5^\circ$ , implying that the metallic Co phases within the CNFs are formed by reduction during carbonization [9]. Characteristic diffraction peaks of Pt/conventional CNFs are observed at  $39.7^\circ$ ,  $46.2^\circ$ ,  $67.5^\circ$ , and  $81.3^\circ$ , corresponding to the (111), (200), (220), and (311) planes of pure Pt phases with a FCC structure (space group  $Fm\bar{3}m[225]$ ). Samples A–C also show the same characteristic peaks, but the peaks observed are of relatively low intensity owing to the high crystallinity of the  $\text{Co}_3\text{O}_4$  phases. Another set of characteristic peaks is observed at  $31.2^\circ$ ,  $36.8^\circ$ ,  $44.8^\circ$ ,  $59.4^\circ$  and  $65.2^\circ$ , corresponding to the (220), (311), (400), (511), and (440) planes, respectively, of  $\text{Co}_3\text{O}_4$  phases with a FCC structure (space group  $Fd\bar{3}m[227]$ ). Furthermore, the intensity of the  $\text{Co}_3\text{O}_4$  phases for samples A–C increases as the size of the  $\text{Co}_3\text{O}_4$  architectures increases. To investigate the chemical bonding states of Co and Pt phases for sample B, XPS analysis measurements were performed as shown in Fig. 3b–c. The binding energies of each spectrum are standardized to the C1s core level ( $\sim 284.5 \text{ eV}$ ). The Co 2p spectra consisting of Co  $2p_{3/2}$  and Co  $2p_{1/2}$  core levels appear at  $\sim 780.3 \text{ eV}$  and  $\sim 795.5 \text{ eV}$ . The energy separation between the Co  $2p_{3/2}$  and Co  $2p_{1/2}$  peaks is  $\sim 15 \text{ eV}$ , in good agreement with a standard  $\text{Co}_3\text{O}_4$  sample [10]. The Co  $2p_{3/2}$  core levels are mainly observed at  $\sim 779.9 \text{ eV}$  and  $\sim 780.7 \text{ eV}$ , corresponding to the binding energies of  $\text{Co}_3\text{O}_4$  and  $\text{Co}(\text{OH})_2$  phases [11,12]. In particular, metal-OH species inhibit CO poisoning on the catalyst's surface by oxidizing adsorbed CO to  $\text{CO}_2$  [13,14]. Reduced CO poisoning results in excellent electro-catalytic activity for DMFCs. As shown in Fig. 3c, the XPS spectra for the Pt 4f core level with Pt  $4f_{7/2}$  and Pt  $4f_{5/2}$  are observed at  $\sim 71.3 \text{ eV}$  and  $\sim 74.6 \text{ eV}$ , respectively, which displays an energy separation of  $3.3 \text{ eV}$  with a theoretical ratio of 4:3. This result implies that Pt states grown on the CNF surface exists mainly in the Pt(0) state. Another set of doublets at  $\sim 72.4 \text{ eV}$  and  $\sim 75.7 \text{ eV}$  correspond to Pt(II) oxidation states such as PtO and  $\text{Pt}(\text{OH})_2$  [15,16]. These results imply that Pt phases loaded on octahedral  $\text{Co}_3\text{O}_4/\text{CNF}$  composites exist mainly in metallic states, which is consistent with the XRD results. Furthermore, for Pt/conventional CNFs and sample B (Fig. 3d and e), the XPS spectra of C 1s show the carbon

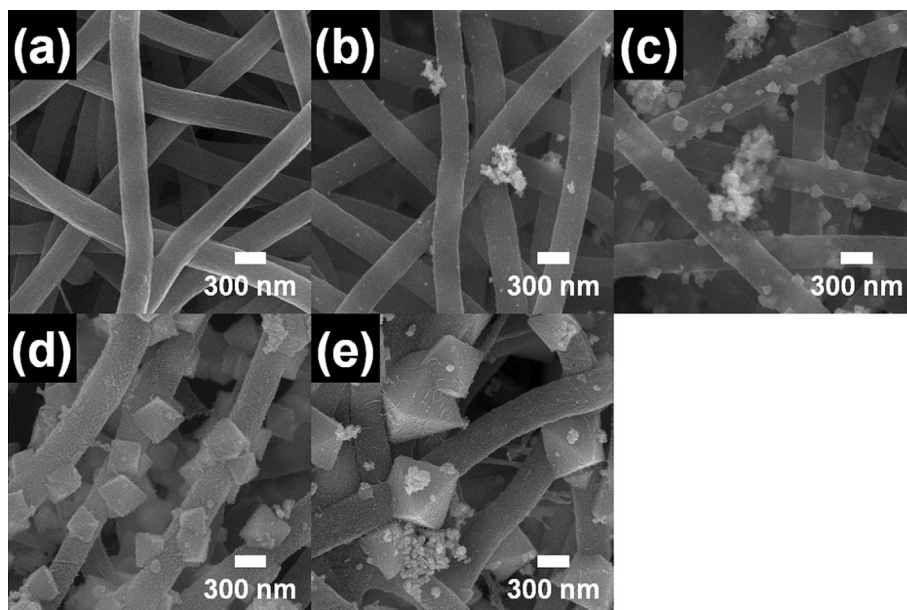


Fig. 1. FESEM images of (a) conventional CNFs, (b) Pt/conventional CNFs, (c) sample A, (d) sample B, and (e) sample C.

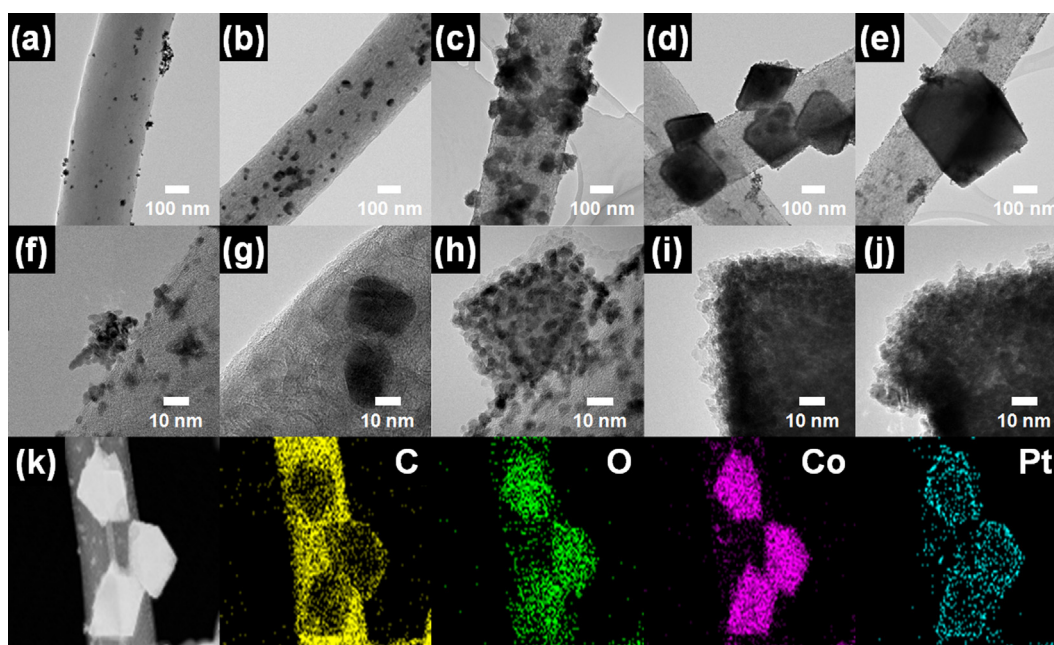
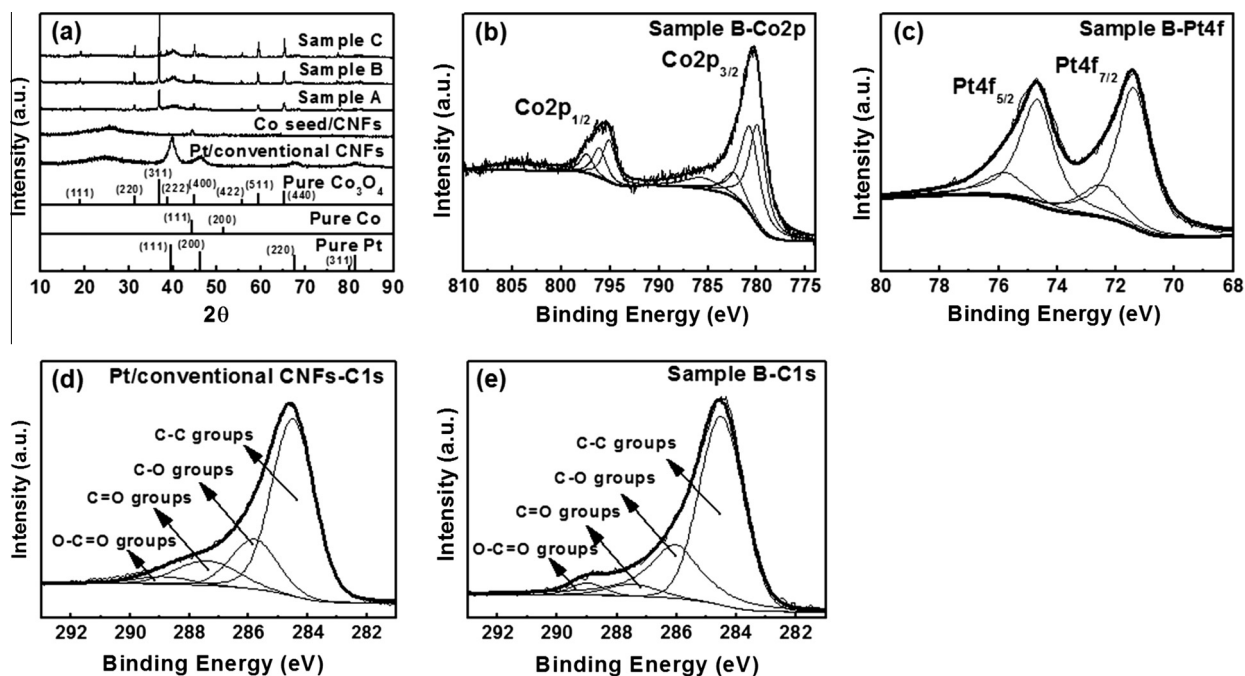


Fig. 2. TEM images (a–e) and enlarged TEM images (f–j) of Pt/CNFs, Co-seed/CNFs, and samples A–C. TEM-EDS mapping data (k) obtained from sample B.

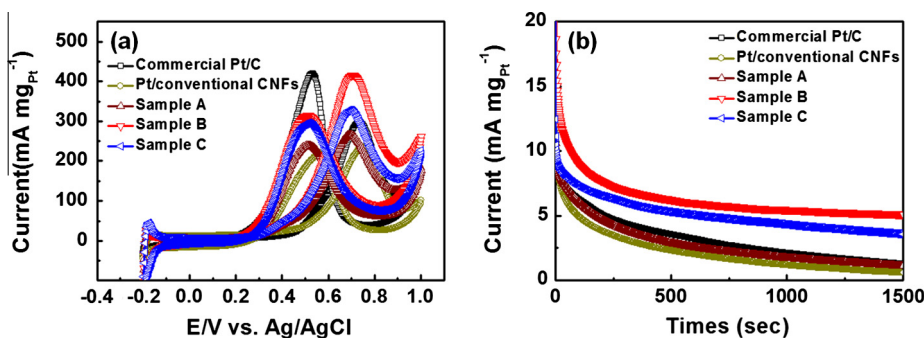
bonding states, namely, C–C ( $\sim 284.5$  eV), C–O ( $\sim 286.0$  eV), C=O ( $\sim 287.4$  eV), and –COO ( $\sim 288.9$  eV) [17]. As C–O groups attach to hydroxyl (–OH) groups, they can easily act as anchoring sites for metal nanoparticles on the carbon matrix [18]. Thus, the percentage of C–O groups of the Pt/conventional CNFs and sample B was 19.3% and 31.9%, respectively, due to the existence of CTAB as a cationic surfactant during the hydrothermal treatment [19]. Therefore, sample B exhibits more superior Pt dispersion on the CNF surface than conventional CNFs due to the increased number of hydroxyl (–OH) groups, which is in good agreement with the FESEM and TEM results.

Fig. 4a shows the cyclic voltammograms (CVs) of methanol electrooxidation with commercial Pt/C, Pt/conventional CNFs, sample A, sample B, and sample C. Methanol and water at the anode

produces electrons, protons, and carbon dioxide, through the following reaction:  $\text{CH}_3\text{OH} + \text{H}_2\text{O} \rightarrow 6\text{e}^- + 6\text{H}^+ + \text{CO}_2$ . Forward anodic peaks and backward anodic peaks are observed at  $\sim 0.68$  V and  $\sim 0.45$  V, respectively. The current density on the forward anodic peak ( $I_f$ ) is attributable to the catalytic activity of the electrode for methanol electrooxidation [20]. The oxidation current densities are  $\sim 296.4$   $\text{mA mg}_{\text{Pt}}^{-1}$  for commercial Pt/C,  $\sim 235.4$   $\text{mA mg}_{\text{Pt}}^{-1}$  for Pt/conventional CNFs,  $\sim 266.0$   $\text{mA mg}_{\text{Pt}}^{-1}$  for sample A,  $\sim 415.6$   $\text{mA mg}_{\text{Pt}}^{-1}$  for sample B, and  $\sim 329.1$   $\text{mA mg}_{\text{Pt}}^{-1}$  for sample C. In particular, sample B displayed the largest increase in methanol electrooxidation, approximately 1.77 and 1.40-fold that of Pt/conventional CNFs and commercial Pt/C, respectively. This improved CV result can be explained by more well-dispersed Pt catalysts loaded on octahedral  $\text{Co}_3\text{O}_4$  as well as the



**Fig. 3.** (a) XRD pattern obtained from Pt/CNFs, Co-seed/CNFs, sample A, sample B, and sample C. XPS spectra of the (b) Co 2p and (c) Pt 4f obtained from sample B. XPS spectra of C1s obtained from (d) Pt/conventional CNFs and (e) sample B.



**Fig. 4.** (a) Cyclic voltammograms (CVs) of methanol electrooxidation/reduction for commercial Pt/C, Pt/conventional CNFs, sample A, sample B, and sample C characterized at a scan rate of  $50 \text{ mV s}^{-1}$  in the range  $-0.2$  to  $1.0 \text{ V}$ . (b) Chronoamperometry of commercial Pt/C, Pt/conventional CNFs, sample A, sample B, and sample C under a constant potential of  $0.5 \text{ V}$  for  $1500 \text{ s}$ .

CNF matrix, implying an increased contact area between electrolyte and catalysts for methanol electrooxidation. The current density on the backward anodic peak ( $I_b$ ) is related to the removal of intermediate species ( $\text{CH}_2\text{OH}$ ,  $\text{CH}_2\text{O}$ ,  $\text{HCOOH}$ , and  $\text{CO}$ ) formed during the forward anodic scan. Therefore, the current ratio of  $I_f$  to  $I_b$  indicates the poison tolerance for methanol electrooxidation [20,21]. A high  $I_f/I_b$  ratio indicates superb poison tolerance resulting from effective removal of intermediate species. The  $I_f/I_b$  ratio of sample B is 1.32, which is higher than that of commercial Pt/C (0.71), Pt/conventional CNFs (1.06), sample A (1.11), and sample C (1.28). Sample B exhibits good tolerance for CO poisoning during methanol electrooxidation due to the existence of  $\text{Co}(\text{OH})_2$  phases [6].

To investigate the electrocatalytic stability of the samples, chronoamperometry measurements were performed under a constant potential of  $0.5 \text{ V}$  over  $1500 \text{ s}$ , as shown in Fig. 4b. The sharp decay in current density during the initial reaction times is due to accumulated intermediate species that can interfere with the catalytic reaction of methanol electrooxidation. Thereafter, the current density decays only slightly until  $1500 \text{ s}$  owing to the

adsorption of  $\text{SO}_4^{2-}$  anions that can hinder the oxidation reaction [22]. In spite of the hindrance of anion adsorption, among all samples, sample B exhibited superior maintenance during methanol oxidation, implying superior electrocatalytic stability due to increased contact area between the electrolyte and Pt catalysts. Therefore, compared to commercial Pt/C and Pt/conventional CNFs, the octahedral  $\text{Co}_3\text{O}_4/\text{CNF}$  composite-supported Pt catalysts achieved greater methanol electrooxidation, which may result from two reasons. First, the Pt catalyst is more well-dispersed on the octahedral  $\text{Co}_3\text{O}_4$  as well as on the CNF matrix. Second,  $\text{Co}(\text{OH})_2$  phases appear to hinder CO poisoning. For this reason, the octahedral  $\text{Co}_3\text{O}_4/\text{CNF}$  composite-supported Pt catalysts are promising catalysts for use in high-performance DMFCs.

#### 4. Conclusions

Octahedral  $\text{Co}_3\text{O}_4/\text{CNF}$  composite-supported Pt catalysts were synthesized using a 3-step process with electrospinning, hydrothermal, and reduction methods. By varying the relative

molar ratio of the Co precursor to the solution over three different values (0.05 M, 0.1 M, and 0.2 M Co precursor), the optimum size of octahedral Co<sub>3</sub>O<sub>4</sub> architectures on the CNF matrix having excellent catalytic activity was found. In particular, sample B exhibited the highest oxidation current density ( $\sim 415.6 \text{ mA mg}_{\text{Pt}}^{-1}$ ) and superb electrocatalytic stability during methanol electrooxidation because of the combined effects of well-dispersed Pt catalysts, owing to optimally sized octahedral Co<sub>3</sub>O<sub>4</sub> on the CNF matrix, and the formation of Co(OH)<sub>2</sub> phases to inhibit CO poisoning.

### Acknowledgements

This work was supported by the International Collaborative Energy Technology R&D Program of the Korea Institute of Energy Technology Evaluation and Planning (KETEP), granted financial resource from the Ministry of Trade, Industry & Energy, Republic of Korea (No. 2138520030800).

### References

- [1] M. Winter, R.J. Brodd, *Chem. Rev.* 104 (2004) 4245–4269.
- [2] G.-H. An, H.-J. Ahn, *J. Electroanal. Chem.* 707 (2013) 74–77.
- [3] S. Sharma, B.G. Pollet, *J. Power Sources* 208 (2012) 96–119.
- [4] J. Zeng, C. Francia, C. Gerbaldi, V. Baglio, S. Specchia, A.S. Aricò, P. Spinelli, *Electrochim. Acta* 94 (2013) 80–91.
- [5] X. Wang, X. Li, D. Liu, S. Song, H. Zhang, *Chem. Commun.* 48 (2012) 2885–2887.
- [6] H. Zhao, Z. Zheng, J. Li, H. Jia, K.-W. Wong, Y. Zhang, W.M. Lau, *Nano-Micro Lett.* 5 (2013) 296–302.
- [7] C. Tan, G. Zhu, M. Hojamberdiev, K. Okada, J. Liang, X. Luo, P. Liu, Y. Liu, *Appl. Catal. B: Environ.* 152–153 (2014) 425–436.
- [8] J.W. Ko, W.-H. Ryu, I.-D. Kim, C.B. Park, *Chem. Commun.* 49 (2013) 9725–9727.
- [9] Y. Aykut, *ACS Appl. Mater. Interfaces* 4 (2012) 3405–3415.
- [10] Z. Chen, S. Chen, Y. Li, X. Si, J. Huang, S. Massey, G. Chen, *Mater. Res. Bull.* 57 (2014) 170–176.
- [11] N. Fischer, M. Minnermann, M. Baeumer, E. Steen, M. Claeys, *Catal. Lett.* 142 (2012) 830–837.
- [12] J.B. Wu, Z.G. Li, X.H. Huang, Y. Lin, *J. Power Sources* 224 (2013) 1–5.
- [13] Z.-B. Wang, P.-J. Zuo, G.-J. Wang, C.-Y. Du, G.-P. Yin, *J. Phys. Chem. C* 112 (2008) 6582–6587.
- [14] L.G. Pereira, F.R. Santos, M.E. Pereira, V.A. Paganin, E.A. Ticianelli, *Electrochim. Acta* 51 (2006) 4061–4066.
- [15] D.-Q. Yang, B. Hennequin, E. Sacher, *Chem. Mater.* 18 (2006) 5033–5038.
- [16] Z. Liu, L. Hong, S.W. Tay, *Mater. Chem. Phys.* 105 (2007) 222–228.
- [17] A.P. Terzyk, *Colloid Surf. A* 177 (2001) 23–45.
- [18] C. Xu, L. Cheng, P. Shen, Y. Liu, *Electrochem. Commun.* 9 (2007) 997–1001.
- [19] A. Stein, Z. Wang, M.A. Fierke, *Adv. Mater.* 21 (2009) 265–293.
- [20] Z. Liu, X.Y. Ling, X. Su, J.Y. Lee, *J. Phys. Chem. B* 108 (2004) 8234–8240.
- [21] Y. Gu, J. Luo, Y. Liu, H. Yang, R. Ouyang, Y. Miao, *J. Nanosci. Nanotechnol.* 15 (2015) 3743–3749.
- [22] G.-H. An, H.-J. Ahn, *ECS Solid State Lett.* 3 (2014) M29–M32.